Frequency Response of Electromagnetic Wave Propagation in Power Tracks

Cexing Wang and Tao Su

School of Electronics and Information Technology
Sun Yat-sen University, Guangzhou, Guangdong, China
wangcx3@mail2.sysu.edu.cn, sutao@mail.sysu.edu.cn

Abstract ─ Previous investigations into the on-chip power distribution network (OCPDN) have focused on low frequency ranges. This study analyzes the high-frequency behavior of OCPDNs, where the wavelength approaches the dimension of the OCPDN and the track structure in the OCPDN. A theoretical model based on transmission line theory with common mode and differential mode analysis is established. The model shows that the power tracks can block the propagation of electromagnetic waves in certain frequency ranges and that wide stopbands exist. Full wave simulation based on (HFSS) is performed to verify the model. The simulation results match the theory, confirming the predicted behavior of the power tracks. Measurements are performed on prototype power tracks and the results are again consistent with the theory. The behavior of the power tracks shown here provides important information for the design of integrated circuits for millimeter-scale wave communications.

Index Terms ─ Frequency response, on-chip power distribution network, pass-band, stop-band.

I. INTRODUCTION

Radio technologies in 5G communication employ millimeter-scale waves [1-3]. High-speed communication with large bandwidth is key to 5G communication. In addition, the stability of integrated circuits must be considered. Part of the on-chip power distribution network (OCPDN) for graphic memory is shown in Fig. 1. The structure consists of equidistant power tracks and shows periodicity in some parts.

The OCPDN may be exposed to signals with frequencies up to 100 GHz in the complex electromagnetic environment. Previous studies have analyzed the electromagnetic interference of power distribution network (PDN) below or close to 1 GHz [4]; however, its behavior in the millimeter-scale wave range is not well understood. Other studies into suppressing OCPDN noise [5-8] typically use extra structures instead of improving the power tracks. Many researchers have treated the problem of OCPDN analysis using numerical approaches with lumped elements. Therefore, a method

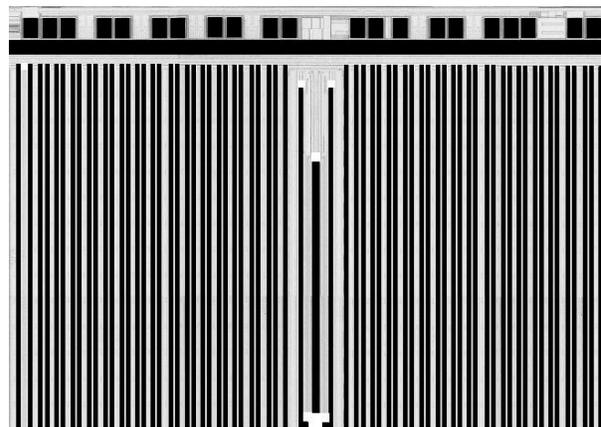of OCPDN analysis at such high frequencies is worth developing.

Fig. 1. Power tracks of the PDN in a memory integrated circuit.

According to [9], the shunt tracks of a periodic structure produce a stopband, which has a Bragg-like effect. In recent years, many studies have attempted to reduce the mutual coupling; for example, by using an electromagnetic band gap structure (EBG) [10, 11] or electromagnetic shielding mesh structure [12]. These periodic structures can block electromagnetic waves. Analyzing the behavior of the PDN by transmission line theory is possible because the space between the source and ground tracks is very small. In this study, we focus on the power tracks. As the wavelength approaches the feature size of the OCPDN, Bloch-like theory can be established to describe the behavior of the OCPDN. The following sections show the development of this theory.

II. THEORETICAL MODEL

A. System model

The power track structure is illustrated in Fig. 2, with some modifications. It consists of metal tracks distributed equidistantly on a ring. Consider the following scenario: a source is connected to the center of the left edge of the ring while a load is connected to the

center of the right edge of the ring. The characteristics of the power track structure for wave propagation can then be described using the ratio of outgoing power on the load to incoming power from the source; i.e., the S_{21} parameter. The objective is to solve the problem using the physical dimensions of wave propagation as well as process-related parameters.
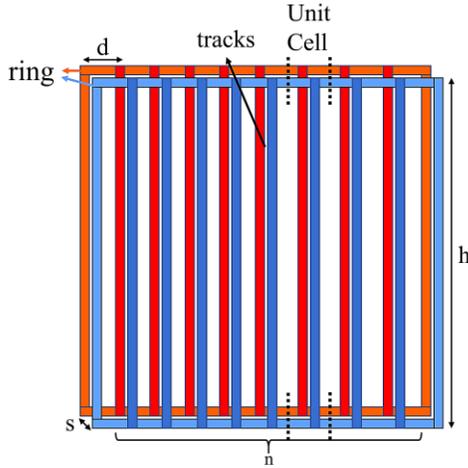

Fig. 2. A schematic model of power tracks.

The structure shows strong periodicity; it can be considered as a sequence of unit cells shown in Fig. 3 (a). As the wavelength of the electromagnetic wave is comparable to the cell dimension, the length of the track is half the wavelength and the interconnection between two tracks (one segment of the ring) is one eighth the wavelength in this paper. The tracks and the segments between two tracks should be considered as transmission lines. Their line impedances and propagation constants are Z_H, β_H and Z_W, k respectively.
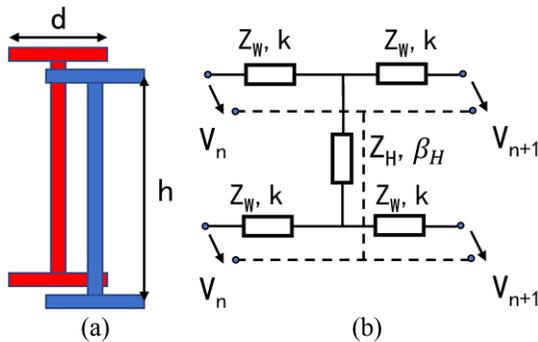

Fig. 3. (a) A unit cell of the power tracks. (b) Equivalent circuit of the unit cell.

The upper and lower parts of the power track are symmetrical. The source and the load are on the axis of symmetry. It is reasonable to consider wave propagation with the common mode method: the upper and lower

edges of the ring have the same voltage distribution, as shown in Fig. 3 (b). Then, the unit cell can be split into two T cells, as shown in Fig. 4 (a), whose behavior is identical. Thus, only one T cell needs to be analyzed.
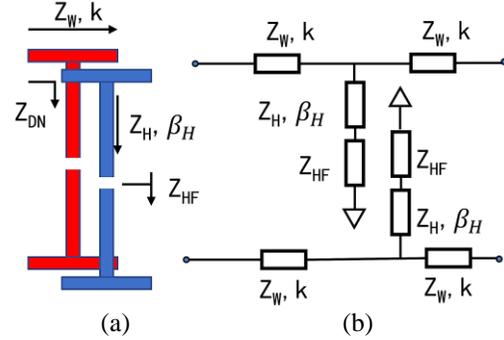

Fig. 4. (a) Two T cells of the unit cell. (b) The transmission line common mode model of the two T cells.

In Fig. 4, Z_{HF} denotes the load impedance viewed from the center of the track down or up. The equivalent impedance of a T cell will be discussed in the next section.

B. Common mode analysis

The behavior of the T cell can be described with an ABCD matrix. Given the cell size, the wave propagation constant and the line impedances, the ABCD matrix can be written into (2) in normalized form. Readers may refer to [13] for deduction details:

$$\begin{bmatrix} V_n \\ I_n \end{bmatrix} = \begin{bmatrix} A & B \\ C & D \end{bmatrix} \begin{bmatrix} V_{n+1} \\ I_{n+1} \end{bmatrix}, \tag{1}$$

$$\begin{bmatrix} A & B \\ C & D \end{bmatrix} =$$
$$\begin{bmatrix} \cos\frac{kd}{2} & j\sin\frac{kd}{2} \\ j\sin\frac{kd}{2} & \cos\frac{kd}{2} \end{bmatrix} \begin{bmatrix} 1 & 0 \\ jZ_W Y_{DN} & 1 \end{bmatrix} \begin{bmatrix} \cos\frac{kd}{2} & j\sin\frac{kd}{2} \\ j\sin\frac{kd}{2} & \cos\frac{kd}{2} \end{bmatrix}. \tag{2}$$

The input impedance of the track, viewed from the ring edge into the track, is Z_{DN} (Fig. 4). For common mode operation, the middle point can be considered as an open, meaning that Z_{HF} equals ∞. Therefore, the input impedance of the track is given as:

$$Z_{DN} = Z_H \frac{Z_{HF} + jZ_H \tan\beta_H\frac{h}{2}}{Z_H + jZ_{HF}\tan\beta_H\frac{h}{2}},$$

$$= Z_H \frac{\infty + jZ_H\tan\beta_H\frac{h}{2}}{Z_H + j\infty\tan\beta_H\frac{h}{2}},$$

$$= \frac{Z_H}{j\tan\beta_H\frac{h}{2}}. \tag{3}$$

The values of k and β_H are equal in the model. Due to the periodicity of the tracks, the propagated wave on the power tracks can be defined as:

$$V_{n+1} = V_n e^{-j\beta d}. \tag{4}$$

Combining (2), (3), and (4) provides the dispersion relationship of the wave propagation in (5). For wave propagation without attenuation, in other words, the solution of $\cos \beta d$ exists in equation (5) and condition (6) should be satisfied. Frequency ranges violating condition (6) correspond to the stopbands:

$$\cos \beta d = \cos kd - \frac{1}{2}\frac{Z_W}{Z_H}\tan\frac{kh}{2}\sin kd, \qquad (5)$$

$$f(k) = \left|\cos kd - \frac{1}{2}\frac{Z_W}{Z_H}\tan\frac{kh}{2}\sin kd\right| < 1. \qquad (6)$$

Equation (6) is transformed into (7) and (8). The passband regions are shown in Fig. 5. In this figure, the horizontal axis is the propagation constant, k, and the vertical axis is the tangent function of k:

$$\frac{1}{2}\frac{Z_W}{Z_H}\tan\frac{kh}{2}\tan\frac{kd}{2} \leq 1, \qquad (7)$$

$$-1 \leq \frac{1}{2}\frac{Z_W}{Z_H}\frac{\tan\frac{kh}{2}}{\tan\frac{kd}{2}}. \qquad (8)$$

The method used for analyzing the power tracks is essentially the transmission line common model method. Further to the above equations, we can also build an equivalent circuit of the power tracks, as shown in Fig. 6, which gives the S_{21} parameter of every frequency.
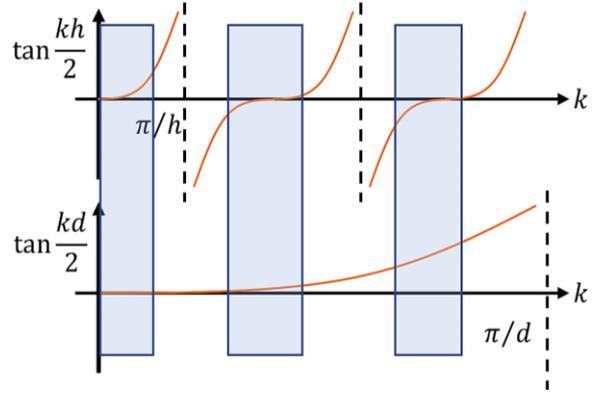

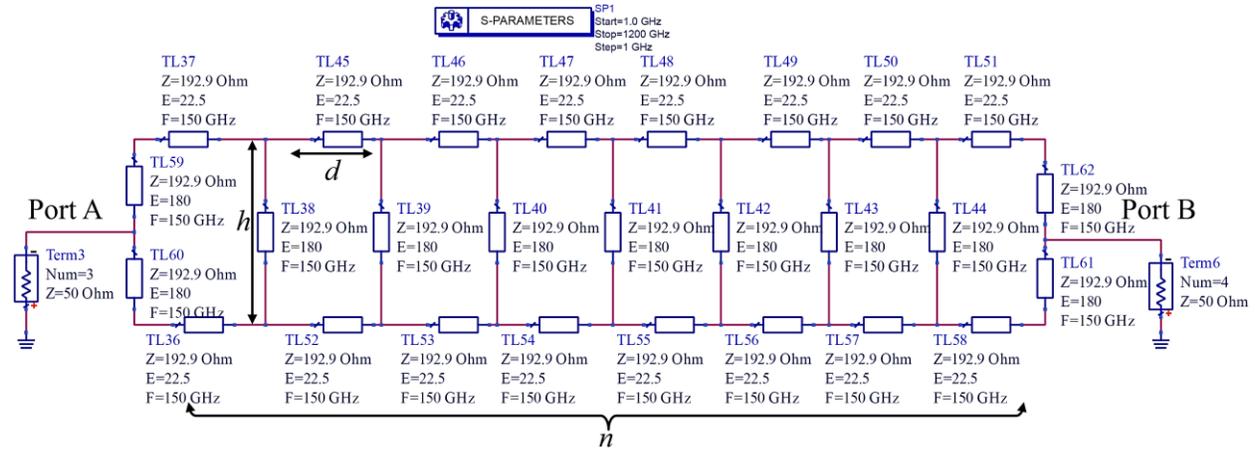Fig. 5. Passband calculated with the common mode method.

Fig. 6. Common mode model of ADS consisting of lossless transmission lines.

C. Differential mode analysis

Common mode wave propagation is an extreme situation with symmetrical ports. Moreover, the ports can be set anywhere on the power tracks, which makes the problem much more complex. Another extreme situation occurs whereby the wave phases in the upper and lower ends of the power tracks are opposite. Then, the two waves meet at the midpoint with a phase difference of 180°. This method is called differential mode, in which the middle point of the power tracks can be considered a short, meaning that Z_{HF} equals 0 as shown in Fig. 7.

For differential mode operation, the input impedance of the track is:

$$Z_{DN} = Z_H \frac{Z_{HF}+jZ_H \tan \beta_H \frac{h}{2}}{Z_H+jZ_{HF}\tan \beta_H \frac{h}{2}},$$

$$= Z_H \frac{0+jZ_H \tan \beta_H \frac{h}{2}}{Z_H+j0 \tan \beta_H \frac{h}{2}},$$

$$= j Z_H \tan \beta_H \frac{h}{2}. \qquad (9)$$

Combining (2), (4), and (9), gives the dispersion relationship of the wave propagation in (10). For wave propagation without attenuation, condition (11) should be satisfied. Frequency ranges violating condition (11) correspond to the stopbands:

$$\cos \beta d = \cos kd + \frac{1}{2}\frac{Z_W}{Z_H}\frac{1}{\tan\frac{kh}{2}}\sin kd, \qquad (10)$$

$$g(k) = \left| \cos kd + \frac{1}{2} \frac{Z_W}{Z_H} \frac{1}{\tan\frac{kh}{2}} \sin kd \right| < 1. \qquad (11)$$

Equation (11) is transformed into (12) and (13). The passband regions are shown in Fig. 8:

$$\frac{1}{2} \frac{Z_W}{Z_H} \frac{1}{\tan\frac{kh}{2}\tan\frac{kd}{2}} \leq 1, \qquad (12)$$

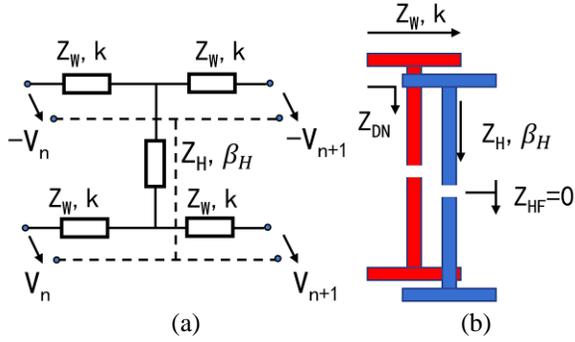$$-1 \leq \frac{1}{2} \frac{Z_W}{Z_H} \frac{\tan\frac{kd}{2}}{\tan\frac{kh}{2}}. \qquad (13)$$

Fig. 7. (a) Voltage distribution, and (b) unit cell of the differential mode.

Through Advanced Design System (ADS) simulation, an ideal differential mode model is built to verify this method. There are two inputs at either end of the left edge, as shown in Fig. 9. The phase difference

between the two input signals is 180°. At any location of the left edge, the source will produce two modes at the same time. According to our theory, the input impedance of the track and the general dispersion relationship is:

$$\Gamma = e^{-j\theta} = \frac{Z_L - Z_0}{Z_L + Z_0}, \qquad (14)$$

$$Z_{DN} = Z_0 \frac{Z_L + jZ_0 \tan \beta_H \frac{h}{2}}{Z_0 + jZ_L \tan \beta_H \frac{h}{2}}, \qquad (15)$$

$$\cos \beta d = \cos kd + \frac{1}{2} j \frac{1 + j a \tan\frac{kh}{2}}{a + j \tan\frac{kh}{2}} \sin kd, \qquad (16)$$

where θ is the voltage phase difference between both ends of the right edge and $a = \frac{1 + e^{-j\theta}}{1 - e^{-j\theta}}$.
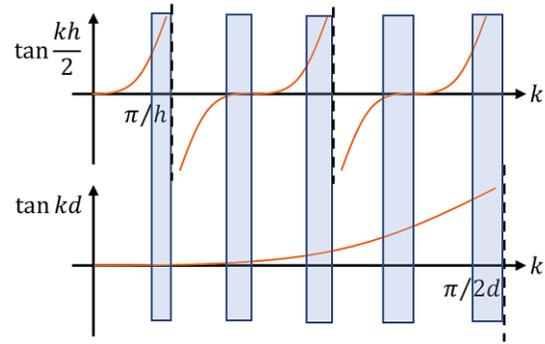

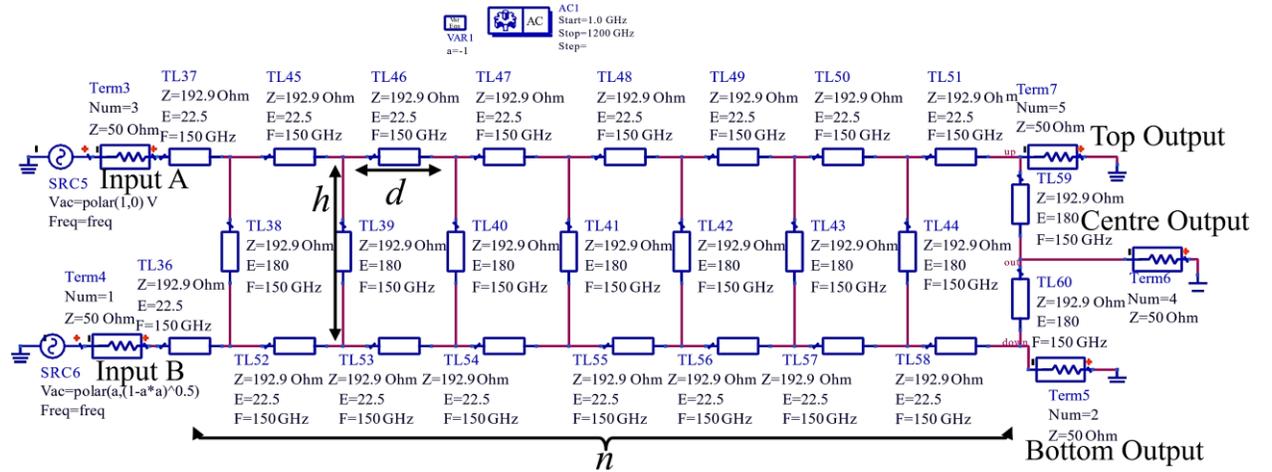Fig. 8. Passband calculated with the differential mode method.

Fig. 9. Differential mode model of ADS consisting of lossless transmission lines.

III. VERIFICATION BY SIMULATION

In this section, we discuss the common-mode and differential-mode behavior and solve the problem of hybrid mode wave propagation. To illustrate this behavior, a simulation with the following parameters is used to verify our model: h represents the length of

power tracks, d is the width of the unit cell, and n represents the number of unit cells. The cross-section of the ring and track are the same. The ring and track have the same line impedance, Z_0, which is equal to 192.924 Ω. Figure 10 compares $f(k)$ and 1 for $h = 1$ mm, $d = 0.125$ mm and n ranges from 7 to 21. According to the common mode

model and equation (6), the frequency ranges where $f(k)$ is above 1 correspond to the stopband, whereas other frequency ranges correspond to the passband. It is expected that the electromagnetic waves of the four bands will be blocked by the power tracks.
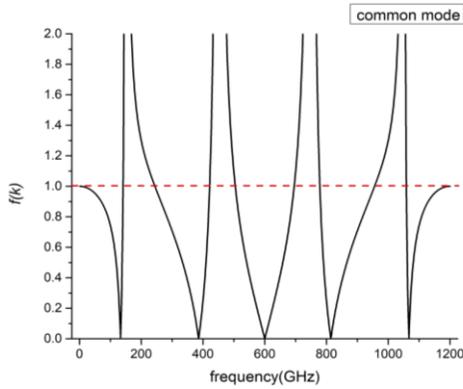

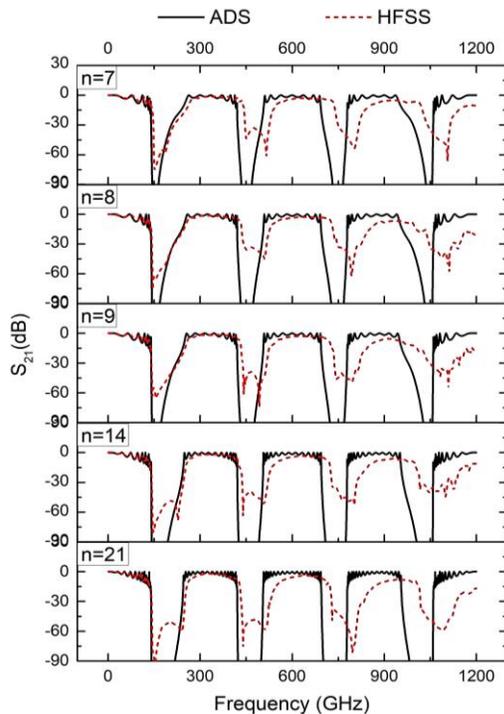Fig. 10. Theoretical result of the common mode model.

Fig. 11. Simulated S_{21} parameter with a variable number of tracks.

Figure 11 shows the simulation results of the common-mode equivalent circuit. It again predicts a stopband very close to the frequency range of the theoretical result. The three-dimensional structure of the power tracks is built using high-frequency structure simulator (HFSS) for full wave simulation. The results are also shown in Fig. 11. The HFSS simulation results

match the ADS simulation results very well, and the two have very close stopbands. In the high-frequency range above 700 GHz, due to the skin effect, the HFSS simulation model impedance mismatch causes greater attenuation. The ranges of the stopband are weakly dependent on the number of unit cells if n is sufficiently large.
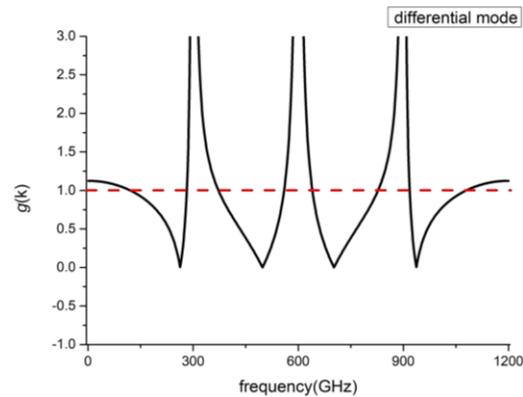

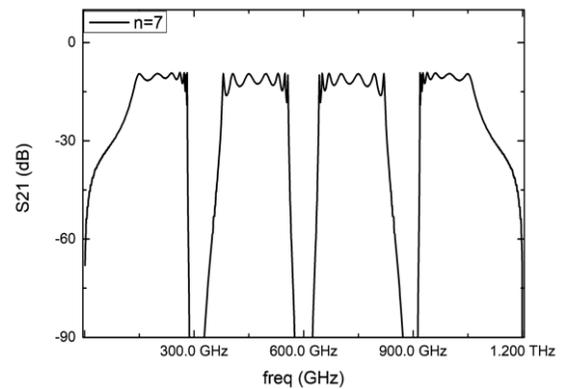Fig. 12. Theoretical result of the differential mode model.

Fig. 13. S_{21} at the top output of the differential mode equivalent circuit in ADS.

Figure 12 compares $g(k)$ and 1. According to the differential mode model and (11), frequency ranges where $g(k)$ is above 1 also correspond to the stopband. In contrast to the common mode, the first stopband is near the DC area. The first passband area is located from approximately 121 GHz to 282 GHz. Figure 13 shows the simulation result of the ideal differential mode equivalent circuit in Fig. 9, which predicts the passbands close to the calculated frequency range. Meanwhile, electromagnetic wave near the DC area is blocked by the differential mode equivalent circuit. It should be noted that the frequency response of the differential mode is an ideal case. In fact, not only differential mode wave propagation but also common mode wave propagation

occurs at the same time. Figure 14 indicates that the differential mode is suppressed at the center output. In contrast to the midpoint, the output located in the rightmost track comprises two modes of guided waves. Therefore, we can predict differential mode behavior by subtracting the behavior at the midpoint.
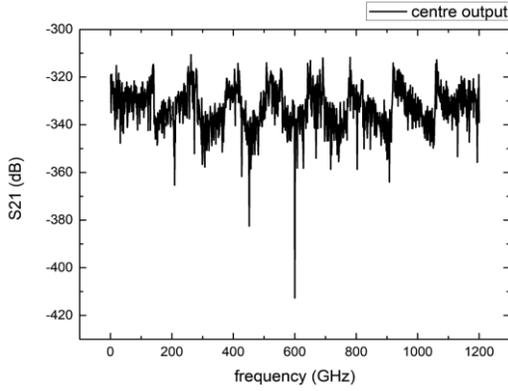

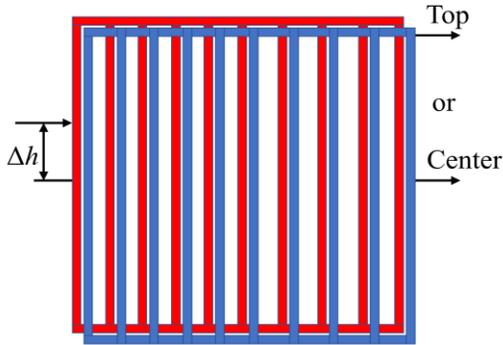Fig. 14. S_{21} at the center output of the differential mode equivalent circuit in ADS.

Fig. 15. Hybrid mode model.

Figure 15 shows the model used to verify the hybrid mode propagation. Δh is the distance between the input location and the midpoint. The port at the top of the right edge collects the hybrid mode information but the midpoint can only collect common mode information. Only one output port is used at a time. The total length of the tracks is 1 mm. Five input locations are set to show the overlap of the hybrid mode. According to the differential mode method, there is no differential mode wave propagation while the input is at the midpoint.

As shown in the theoretical result and equivalent circuit simulation, the power of electromagnetic waves near 0 GHz, 300 GHz, 600 GHz, 900 GHz, or 1200 GHz are blocked by the differential mode method. Directly measuring the wave conduction of the differential mode is difficult; thus, equation (17) verifies the existence of the power of the differential mode:

$$\Delta |S_{21}|^2 = \left| S_{21hybrid} \right|^2 - \left| S_{21common} \right|^2. \qquad (17)$$

The subtraction results from ADS and HFSS simulations are shown in Fig. 16. By subtracting the common mode EM wave, the results also show the stopbands near 0 GHz, 300 GHz, 600 GHz, 900 GHz, and 1200 GHz.
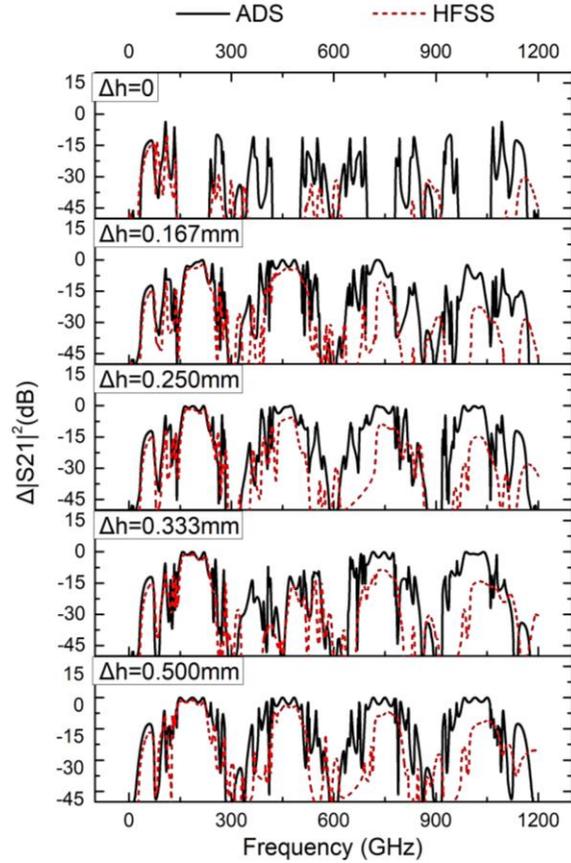

Fig. 16. $|S_{21top}|^2 - |S_{21center}|^2$ of simulations with a variable input distance.

IV. VERIFICATION BY MEASUREMENT

In this section, geometrical scale model measurements [14] based on a printed circuit board (PCB) shown in Fig. 17 are compared with transmission line mode in ADS. The common mode test corresponds to port1 and port3, and the hybrid mode test corresponds to port2 and port4. With the following parameters: $h = 100$ mm, d= 12.5 mm, $n = 7$, and relative permittivity of the dielectric substrate is equal to 4.5, the first stopband of the common mode ranges from 0.8 to 1.3 GHz, according to the theory. By referring to [15], the attenuations can be calculated by the following equation:

$$\alpha \left[\frac{dB}{m} \right] = \frac{20\pi}{ln10} \frac{1}{Q_c \lambda_g}, \qquad (18)$$

Q_c represents the quality factor at the resonant frequency and λ_g is the wavelength in the power tracks.

In the measurement, the effective permittivity is equal to 3.3, loss coefficient is equal to 3.66 dB/m, and dielectric loss angle tangent is equal to 0.05.
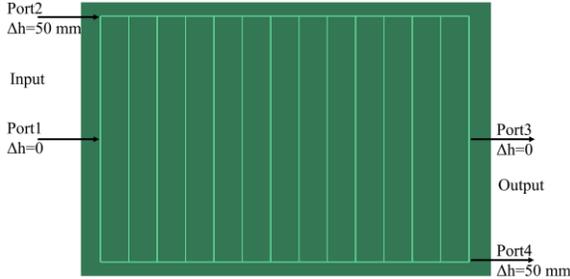

Fig. 17. Prototype of power tracks based on a printed circuit board.
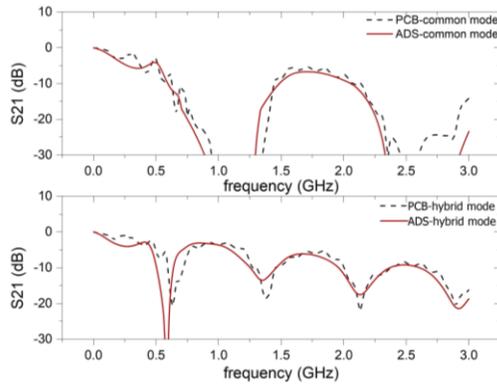

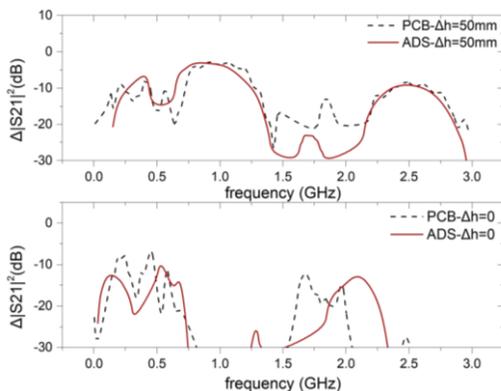Fig. 18. Measurement and ADS results of common mode and hybrid mode methods.

Fig. 19. Subtraction results of common mode and hybrid mode methods.

As shown in Fig. 18, the first stopband is very close to the frequency range and the second stopband also obeys the common mode theory. In Fig. 18, the hybrid

mode measurement shows a different frequency response from the common mode and differential mode methods. To confirm the existence of the differential mode, this section calculates the power and squares S_{21} to obtain the result of the mixed-mode power minus the common-mode power in the simulation and experiment, respectively. Figure 19 shows the subtraction results from the measurement and transmission line model for $\varepsilon_{eff} = 3.3$, $\alpha = 3.66$ dB/m, and $\tan\delta = 0.05$. According to the differential mode theory, the above simulation shows the passband near 200 GHz, which corresponds to 1.2 GHz from the measurement. We verify that the power can split into two modes. If the input or output is set at the midpoint, no differential mode propagation occurs in the measurement either.

V. CONCLUSION

The propagation of electromagnetic waves in power tracks consists of two modes: common mode and differential mode. The first stopband of the common mode is where the wavelength is about twice the track length. The first stopband of the differential mode is where the wavelength is more than twice the track length. The widths of the stopband increase with the number of tracks and become saturated as the track number exceeds nine. Equations are presented for calculating the exact range of the stopbands. The frequency response of propagation in the power tracks in the general case is a combination of common-mode behavior and differential-mode behavior; it varies with the location of the source and observation points. If the source or observation point is located at the center of the power tracks, there will be no differential mode. However, because the stopbands of the two modes have an overlap, there is always a stopband for the propagation.

Employing equivalent circuits based on transmission line theory is an effective method for analyzing power tracks, as proved with field simulations and practical measurements. The frequency response of the power track reveals the millimeter-scale wave electromagnetic properties of on-chip power distribution networks. Our future study will work on more complex mesh structure. It also aids the development of new structures for millimeter-scale wave filter design.

REFERENCES

[1] P. A. Dzagbletey and Y. Jung, "Stacked microstrip linear array for millimeter-wave 5G baseband communication," *IEEE Antennas Wirel. Propag. Lett.*, vol. 17, no. 5, pp. 780-783, May 2018.

[2] S. Zhu, H. Liu, Z. Chen, and P. Wen, "A compact

gain-enhanced vivaldi antenna array with suppressed mutual coupling for 5G mm wave application," *IEEE Antennas Wirel. Propag. Lett.*, vol. 17, no. 5, pp. 776-779, May 2018.

[3] C. Choi, J. H. Son, O. Lee, and I. Nam, "A +12-dBm OIP3 60-GHz RF downconversion mixer with an output-matching, noise- and distortion-canceling active balun for 5G applications," *IEEE Microw. Wirel. Compon. Lett.*, vol. 27, no. 3, pp. 284-286, Mar. 2017.

[4] C. Yoon, et al., "A slope and amplitude controllable triangular-current generator for the injection of a broad-band PDN noise," *IEEE Electromagn. Compat. Mag.*, vol. 5, no. 4, pp. 112-116, Fourth Quarter 2016.

[5] J. Cho, Y. Kim, J. Kim, V. Sundaram, and R. Tummala, "Analysis of glass interposer PDN and proposal of PDN resonance suppression methods," *2013 IEEE International 3D Systems Integration Conference (3DIC)*, San Francisco, CA, pp. 1-5, 2013.

[6] K. Cho, et al., "Design and analysis of power distribution network (PDN) for high bandwidth memory (HBM) interposer in 2.5D terabyte/s bandwidth graphics module," *2016 IEEE 66th Electronic Components and Technology Conference (ECTC),* Las Vegas, NV, pp. 407-412, 2016.

[7] S. Kim, Y. Kim, K. Cho, J. Song, and J. Kim, "Design and measurement of a novel on-interposer active power distribution network for efficient simultaneous switching noise suppression in 2.5-D/3-D IC," *IEEE Trans. Compon., Packag. Manuf. Technol.*, in press.

[8] H. Kim, S. Kim, J. Kim, C. Yoon, B. Achkir, and J. Fan, "On-chip linear voltage regulator module (VRM) effect on power distribution network (PDN) noise and jitter at high-speed output buffer," in *IEEE Electromagn. Compat. Mag.*, vol. 4, no. 2, pp. 108-113, Second Quarter 2015.

[9] C. Caloz and T. Itoh, *Electromagnetic Metamaterials: Transmission Line Theory and Microwave Applications*. Wiley-IEEE Press, 2006.

[10] I. Mazraeh-Fard, et al., "Design of a planar surface wave antenna with a bidirectional pattern based on periodic structures for telemetry applications," *Applied Computational Electromagnetics Society Journal*, vol. 31, no. 12, pp. 1431-1438, 2016.

[11] T. Jiang, T. Jiao, and Y. Li, "A low mutual coupling mimo antenna using periodic multi-layered electromagnetic band gap structures," *Applied Computational Electromagnetics Society Journal*, vol. 33, no. 3, pp. 305-311, 2018.

[12] H. M. El-Maghrabi, "Electromagnetic shielding effectiveness calculation for cascaded wire-mesh-screens with glass substrate," *Applied Computa-tional Electromagnetics Society Journal*, vol. 33, no. 6, pp. 641-647, 2018.

[13] D. M. Pozar, *Microwave Engineering*. John Wiley & Sons, Inc., New York, 2012.

[14] C. A. Balanis, K. Zhang, and C. R. Birtcher, "Geometrical scale modeling of gain and echo area: simulations, measurements and comparisons," *Applied Computational Electromagnetics Society Journal*, vol. 33, no. 1, pp. 95-98, Jan. 2018.

[15] R. A. Pucel, "Design considerations for monolithic microwave circuits," in *IEEE Transactions on Microwave Theory and Techniques*, vol. 29, no. 6, pp. 513-534, June 1981.

Cexing Wang received the B.S. degree in Electrical Engineering from Sun Yat-sen University, Guangzhou, China, in 2017, where he is currently pursuing the M.S. degree.

His current research interests include the analysis of frequency response in OCPDN and filter design based on periodic structure.

Tao Su was born in Yiyang, China, in 1977. He received the B.Sc. degree in Physics from the University of Science and Technology of China, Hefei, China, in 2000, the M.Sc. degree in Microwave Engineering from the Munich University of Technology, Munich, Germany, in 2005, and the Doktor-Ingenieur degree in Electronic Engineering from the University of Erlangen-Nurnberg, Erlangen, Germany, in 2009.

He worked as a Doctor Student with Infineon Technologies AG, Munich, from 2006 to 2009. He is now an Associate Professor in the School of Electronics and Information Technology at Sun Yat-sen University, Guangzhou, China. His current research interest is the integrated circuits design.